



OPEN

# Possible ferroelectricity in perovskite oxynitride $\text{SrTaO}_2\text{N}$ epitaxial thin films

## SUBJECT AREAS:

FERROELECTRICS AND  
MULTIFERROICS

SOLID-STATE CHEMISTRY

ELECTRONIC MATERIALS

ELECTRONIC PROPERTIES AND  
MATERIALSReceived  
16 October 2013Accepted  
28 April 2014Published  
16 May 2014Correspondence and  
requests for materials  
should be addressed toY.H. (hirose@chem.s.  
u-tokyo.ac.jp)Daichi Oka<sup>1</sup>, Yasushi Hirose<sup>1,2,3</sup>, Hideyuki Kamisaka<sup>1,3</sup>, Tomoteru Fukumura<sup>1,2,3</sup>, Kimikazu Sasa<sup>4</sup>, Satoshi Ishii<sup>4</sup>, Hiroyuki Matsuzaki<sup>5</sup>, Yukio Sato<sup>6</sup>, Yuichi Ikuhara<sup>6</sup> & Tetsuya Hasegawa<sup>1,2,3</sup>

<sup>1</sup>Department of Chemistry, School of Science, The University of Tokyo, 7-3-1 Hongo, Bunkyo, Tokyo 113-0033, Japan, <sup>2</sup>Kanagawa Academy of Science and Technology (KAST), 3-2-1 Sakado, Takatsu, Kawasaki 213-0012, Japan, <sup>3</sup>CREST, Japan Science and Technology Agency, 7-3-1 Hongo, Bunkyo, Tokyo 113-0033, Japan, <sup>4</sup>Tandem Accelerator Complex, University of Tsukuba, 1-1-1 Tennodai, Tsukuba, 305-8577, Japan, <sup>5</sup>Department of Nuclear Engineering and Management, School of Engineering, The University of Tokyo, 2-11-16 Yayoi, Bunkyo, Tokyo 113-0032, Japan, <sup>6</sup>Institute of Engineering Innovation, The University of Tokyo, 2-11-16 Yayoi, Bunkyo, Tokyo 113-8656, Japan.

Compressively strained  $\text{SrTaO}_2\text{N}$  thin films were epitaxially grown on  $\text{SrTiO}_3$  substrates using nitrogen plasma-assisted pulsed laser deposition. Piezoresponse force microscopy measurements revealed small domains ( $10^1$ – $10^2$  nm) that exhibited classical ferroelectricity, a behaviour not previously observed in perovskite oxynitrides. The surrounding matrix region exhibited relaxor ferroelectric-like behaviour, with remanent polarisation invoked by domain poling. First-principles calculations suggested that the small domains and the surrounding matrix had *trans*-type and a *cis*-type anion arrangements, respectively. These experiments demonstrate the promise of tailoring the functionality of perovskite oxynitrides by modifying the anion arrangements by using epitaxial strain.

Perovskite oxynitrides have attracted much attention because of their novel electronic functionalities, such as visible light absorption<sup>1</sup>, photocatalytic activity<sup>2</sup>, colossal magneto-resistance<sup>3</sup>, and high dielectric constant<sup>4</sup>. These features presumably originate from the concomitant interaction between oxygen and nitrogen ions, which have different ionicities/valencies<sup>5</sup>. The electronic functionalities of perovskite oxynitrides may also be influenced by the geometrical configuration of the O and N atoms around their metal cations. For  $\text{ABO}_2\text{N}$ -type oxynitrides, in which each B cation is surrounded by four O and two N ions, there are two possible anion configurations: the two nitrogen ions can occupy either adjacent (*cis*-type) or opposite (*trans*-type) sites in a  $\text{BO}_4\text{N}_2$  octahedron. Researchers have argued that the dielectric properties of  $\text{ABO}_2\text{N}$  are related to anion arrangement<sup>6–8</sup>: for example, Page *et al.* suggested that ferroelectricity in *trans*-type anion-ordered  $\text{ATaO}_2\text{N}$  ( $\text{A} = \text{Sr}$  and  $\text{Ba}$ ) phases may be caused by the off-centre displacement of Ta ions. They investigated this concept by theoretically studying the stability of phases with different nitrogen arrangements and space groups<sup>6</sup>. However, *trans*-type phases in this system are less energetically stable than *cis*-type phases<sup>6</sup>, and bulk  $\text{SrTaO}_2\text{N}$  specimens have been confirmed to exhibit *cis*-type configurations (Fig. 1a)<sup>7,8</sup>. As suggested by Page *et al.*<sup>6</sup>, the ferroelectric *trans*-type phase would be stabilised by compressive epitaxial stress because of induced tetragonal distortion (Fig. 1b). Such metastable ferroelectricity was not observed in an epitaxial thin film of compressively strained  $\text{BaTaO}_2\text{N}$  deposited on a  $\text{SrRuO}_3$ -buffered  $\text{SrTiO}_3$  (STO) substrate<sup>9</sup>. This lack of ferroelectricity was likely caused by the considerably relaxed  $\text{BaTaO}_2\text{N}$  lattice, indicated by the small lattice distortion ( $c/a = 1.0099$ ) generated by the large lattice mismatch ( $-4.7\%$ ) between the film ( $a = 4.1125 \text{ \AA}^4$ ) and the  $\text{SrRuO}_3$  buffer layer ( $a = 3.92 \text{ \AA}$ ; pseudo-cubic approximation<sup>10</sup>). To apply enough tetragonal distortion to produce ferroelectric behaviour,  $\text{SrTaO}_2\text{N}$  is a more suitable film than  $\text{BaTaO}_2\text{N}$ , because the lattice constant of  $\text{SrTaO}_2\text{N}$  ( $a = 4.03 \text{ \AA}$ ; pseudo-cubic approximation<sup>11</sup>) produces a better lattice match ( $-3.1\%$ ) to the STO ( $a = 3.905 \text{ \AA}$ ) substrate.

In the present paper, we report room-temperature ferroelectricity in compressively strained  $\text{SrTaO}_2\text{N}$  thin films epitaxially grown on STO single-crystal substrates. Local piezoresponse measurements revealed the incorporation of small classical ferroelectric domains with dimensions of  $10^1$ – $10^2$  nm in a relaxor ferroelectric-like matrix. The ferroelectric domains and the relaxor-like matrix were identified as *trans*- and *cis*-type phases, respectively, based on results of first-principles density functional theory (DFT) calculations that mapped the total energy of  $\text{SrTaO}_2\text{N}$  for various lattice parameters.

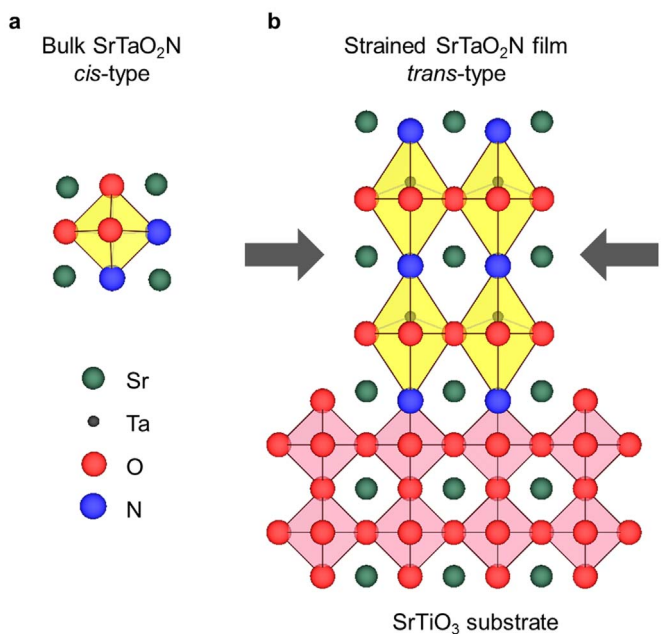


**Figure 1 | Schematic illustration of anion arrangement in  $\text{SrTaO}_2\text{N}$ .** (a) Unstrained bulk  $\text{SrTaO}_2\text{N}$  with a *cis*-type anion arrangement<sup>7,8</sup>. (b) Tetragonally strained  $\text{SrTaO}_2\text{N}$  thin film with a *trans*-type anion arrangement epitaxially stabilised on the  $\text{SrTiO}_3$  substrate. The structures were drawn by VESTA<sup>27</sup>.

## Results

**Epitaxial growth of  $\text{SrTaO}_2\text{N}$  thin films.**  $\text{SrTaO}_{3-x}\text{N}_x$  thin films were grown on the (100) planes of STO single-crystal substrates using nitrogen plasma-assisted pulsed laser deposition (NPA-PLD). The nitrogen content,  $x$ , in these films, was evaluated by nuclear reaction analysis (NRA);  $x$  had a range from 0 to  $\sim 1.2$ , depending on the partial pressure of the supplied nitrogen gas and the deposition rate of the film (Supplementary Fig. S1). X-ray diffraction (XRD) confirmed that pure perovskite  $\text{SrTaO}_{3-x}\text{N}_x$  films grew epitaxially on the STO substrates despite the wide variation in nitrogen content (Supplementary Fig. S2). The tetragonal lattice parameters,  $a$  and  $c$ , and the unit cell volume,  $V$ , of the  $\text{SrTaO}_{3-x}\text{N}_x$  thin films monotonically increased with increasing  $x$  (Fig. 2a and 2b). Near the stoichiometric composition [ $x = 1.02(6)$ ], we observed a  $V$  of  $65.385 \text{ \AA}^3$ , agreeing well with the reported lattice volume of bulk  $\text{SrTaO}_2\text{N}$  ( $65.478 \text{ \AA}^3$ )<sup>4</sup>. The cation stoichiometry of this film was confirmed by Rutherford backscattering spectrometry (RBS) (Supplementary Fig. S3). In addition, we confirmed the band gap energy of  $2.27 \text{ eV}$  (Fig. 2c) determined from a plot of  $(\alpha h\nu)^2$  versus  $h\nu$ , which agreed well with a previously reported value ( $2.3 \text{ eV}$ )<sup>12</sup>. Later, we shall discuss the crystal structure and physical properties of stoichiometric  $\text{SrTaO}_{3-x}\text{N}_x$  thin films with nitrogen compositions of  $x = 1.00 \pm 0.06$ , which we refer to hereafter as  $\text{SrTaO}_2\text{N}$ .

Investigating the microstructure of the  $\text{SrTaO}_2\text{N}$  films using transmission electron microscopy (TEM; Fig. 2d) and high-angle annular dark field scanning TEM (HAADF-STEM; Fig. 2e), we found a sharp film/substrate interface and a uniform perovskite lattice structure with no segregation. Using XRD, we investigated the tetragonal lattice distortions of the  $\text{SrTaO}_2\text{N}$  thin films. Despite the partially relaxed lattice of the thin films (the representative reciprocal space map shown in the inset of Fig. 2b), the tetragonal distortion ratio of  $c/a$  reached  $1.026$  ( $a = 3.98 \text{ \AA}$ ;  $c = 4.08 \text{ \AA}$ ) at a film thickness of  $20 \text{ nm}$ . The  $c/a$  ratio decreased with increasing film thickness, becoming nearly constant ( $\sim 1.013$ ) in the films thicker than  $100 \text{ nm}$ . These results indicate that the  $\text{SrTaO}_2\text{N}$  epitaxial thin films were highly strained and distorted, especially near the film/substrate interface, compared with bulk

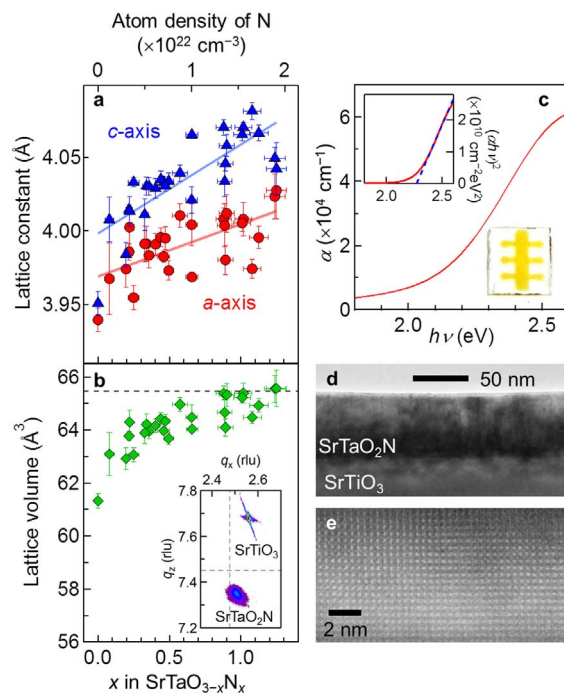


**Figure 2 | Structure of the  $\text{SrTaO}_{3-x}\text{N}_x$  epitaxial thin films.** (a) In-plane (circles) and out-of-plane (triangles) lattice constants of the  $\text{SrTaO}_{3-x}\text{N}_x$  thin films as a function of nitrogen content,  $x$ . The solid lines are guides to the eye, representing a linear relationship. (b) Lattice volume calculated from (a). The dashed line shows the lattice volume of bulk  $\text{SrTaO}_2\text{N}$ <sup>4</sup>. The inset shows an XRD reciprocal space map of the 103 diffraction of the  $\text{SrTaO}_2\text{N}$  thin film and STO substrate. The dotted lines represent the lattice constant of bulk  $\text{SrTaO}_2\text{N}$ , derived from Ref. 4. (c) Absorption coefficients calculated from the extinction coefficients. The left inset is a plot of  $(\alpha h\nu)^2$  versus  $h\nu$  (solid line) and linear fitting results (dashed line). The right inset is a photograph of a patterned  $\text{SrTaO}_2\text{N}$  thin film grown on a  $\text{SrTiO}_3$  substrate demonstrating visible light absorption. (d) Low-magnification cross-sectional TEM image of the  $\text{SrTaO}_2\text{N}$  film. (e) High-magnification HAADF-STEM image of the  $\text{SrTaO}_2\text{N}$  film.

$\text{SrTaO}_2\text{N}$  ( $c/a \sim 1.002$ ) and  $\text{BaTaO}_2\text{N}$  epitaxial thin films ( $c/a \sim 1.009$ )<sup>9</sup>. We also confirmed that  $\text{SrTaO}_2\text{N}$  epitaxial thin films were perfectly relaxed ( $c/a \sim 1.002$ ) on  $(\text{LaAlO}_3)_{0.3}(\text{Sr}_2\text{AlTaO}_6)_{0.7}$  substrate ( $a = 3.868 \text{ \AA}$ ) with larger lattice mismatch ( $-4.0\%$ ) than STO.

**Investigation of ferroelectricity in  $\text{SrTaO}_2\text{N}$  epitaxial thin films.** The ferroelectricity of the  $\text{SrTaO}_2\text{N}$  thin films was investigated using contact-resonance mode vertical piezoresponse force microscopy (VPFM)<sup>13</sup>, which probes the out-of-plane piezoresponse of the film. VPFM measurements were conducted under vacuum ( $< 10 \text{ Pa}$ ) at room temperature. In the virgin state, small domains (size range from tens to hundreds of nanometers) in the thin film produced much larger piezoresponse than did the surrounding regions (Fig. 3a and 3b). To investigate these locally varying ferroelectric properties, we performed switching spectroscopic measurements, in which we recorded the piezoresponse of the remanent polarisation as a function of the amplitude of the preceding switching DC voltage pulse (Fig. 3c)<sup>14</sup>. The curves of local piezoresponse versus DC bias exhibited clear hysteresis (Fig. 3d) in the domains that exhibited large piezoresponse in the virgin state (point A in Fig. 3b). The amplitude components of the curve were butterfly shaped (Fig. 3e) and the phase components exhibited sharp  $180^\circ$  inversions at the coercive fields (Fig. 3f). These features denote the presence of classical ferroelectricity, which has never before been observed in perovskite oxynitrides to our knowledge. The surrounding regions with negligible piezoresponse in the virgin state (point B

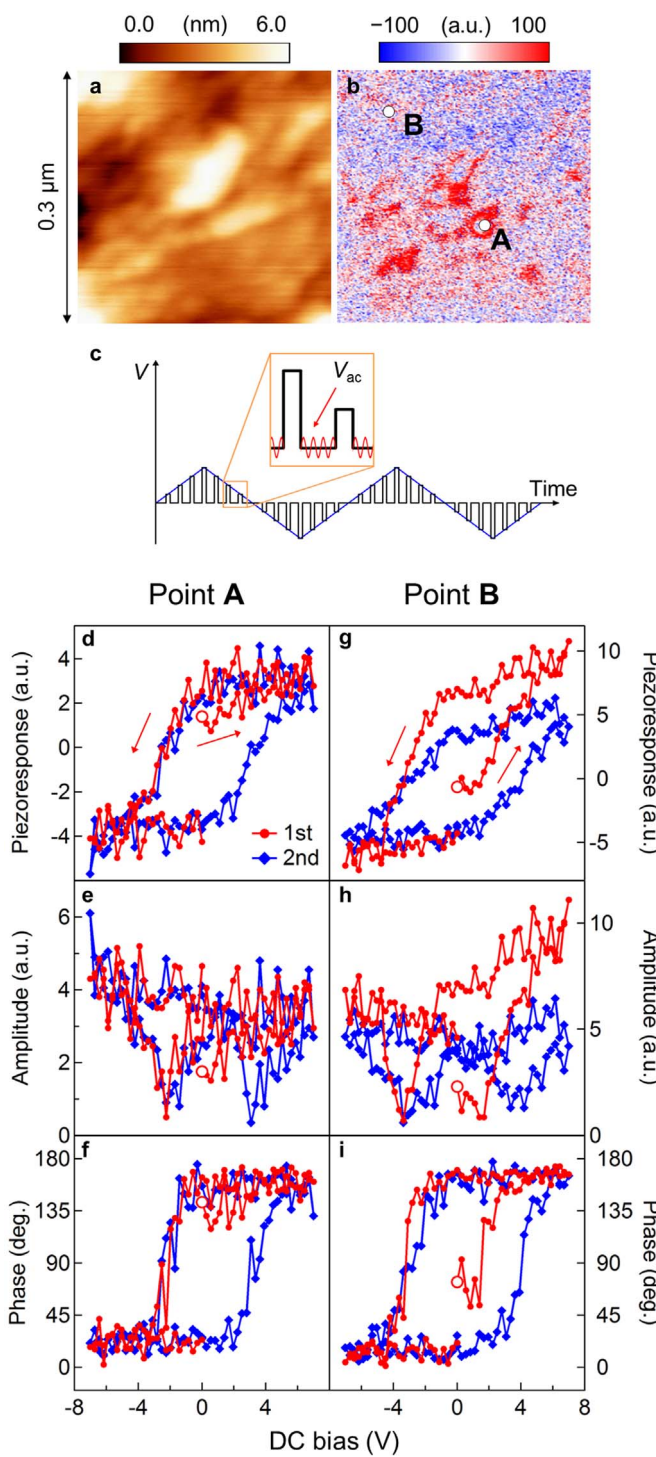


**Figure 3 | Local ferroelectric behaviour of the SrTaO<sub>2</sub>N epitaxial thin film.** (a) Topographic and (b) piezoresponse ( $A \cos\theta$ ) images of the SrTaO<sub>2</sub>N thin film (thickness = 288 nm). (c) Schematic illustration of the switching DC pulses and probing AC waves in switching spectroscopy measurements. After each DC pulse, the piezoresponse originating from the remanent polarisation is probed with a small AC bias. (d)–(i) Local piezoresponse examined by switching spectroscopy with an AC bias of  $\pm 1$  V at positions A [(d)–(f)] and B [(g)–(i)] indicated in (b). Open circles represent the initial point of the measurements. (e), (f) and (h), (i) present amplitude and phase components of (d), (g), respectively.

in Fig. 3b) exhibited an apparent hysteretic piezoresponse induced by the external DC bias (Fig. 3g–3i). The piezoresponse of the SrTaO<sub>2</sub>N films was much weaker than those of conventional ferroelectric

materials. The weaker response may have been caused by the small piezoelectric constant of SrTaO<sub>2</sub>N, but it may also be possible that the region near the film/substrate interface was only ferroelectric because of lattice relaxation, as discussed in the previous section.

To investigate the unusual hysteretic behaviour observed in the matrix region, we took a series of VPFM images from the same region over time after performing domain poling<sup>15,16</sup>. In the virgin state before poling, the piezoresponse signals were hardly detectable (Fig. 4b) because the measured area was much larger than the size of the ferroelectric domains (tens to hundreds of nanometers). Immediately after poling, the induced piezoresponse was clearly different between the positively and negatively poled regions (Fig. 4e), and there was a  $180^\circ$  phase difference between the two distinct domains, indicating perfect polarisation inversion (Fig. 4c and 4d). The induced polar domains began to relax within 1 h, and the contrast between the domains weakened considerably after 8 h (Fig. 4f–4i); in contrast, the surface morphology did not change over time (Fig. 4a). Such relaxation behaviour is typical in relaxor materials and has been observed in lead lanthanum zirconate titanate ceramics<sup>17</sup>.

Interpreting these results must be done with caution, however: recent PFM studies on oxides reported that even paraelectric materials, such as TiO<sub>2</sub> thin films and heterostructures such as LaAlO<sub>3</sub>/SrTiO<sub>3</sub>, can exhibit spurious relaxor-like behaviour, caused by remanent piezoresponses generated from external-electric field-induced motion of ionic species<sup>18,19</sup>. To check for this possibility, we examined how the dielectric constants of our thin films depended on temperature (Fig. 5). We found no significant signs of ferroelectric–paraelectric phase transitions up to 600 K, at which point the sample began to be oxidised, as confirmed by XRD (data not shown). However, the real part of the dielectric constant,  $\epsilon'$ , from 20 Hz to 10 kHz, exhibited positive  $d\epsilon'/dT$ , as seen in conventional “intrinsic” relaxors<sup>20</sup>. In contrast, in “extrinsic” relaxors,  $d\epsilon'/dT$  tends to decrease with increasing temperature<sup>21</sup>. Thus, we tentatively conclude that the majority of the present SrTaO<sub>2</sub>N film surrounding the small domains (i.e., the relaxor-like matrix region) is an intrinsic relaxor.

To investigate the possibility of ferroelectric–paraelectric phase transitions in the matrix region, we also conducted high-temperature XRD. To avoid oxidation, the SrTaO<sub>2</sub>N film was capped with  $\sim 20$  nm of amorphous LaAlO<sub>3</sub>. Figure 6 shows the measured lattice constants as a function of temperature, clearly indicating an inflection at  $\sim 600$  K in both the *a*- and *c*-axis lengths. Choi *et al.* reported similar behaviour in BaTiO<sub>3</sub> ferroelectric thin films at their Curie temperature<sup>22</sup>, leading us to speculate that the inflection point in the present SrTaO<sub>2</sub>N epitaxial thin film corresponds to its Curie temperature.

Based on these findings, we believe that our SrTaO<sub>2</sub>N film contained classical ferroelectric domains ( $10^1$ – $10^2$  nm) and a surrounding matrix with a relaxor-like nature, although we observed hysteretic behaviour only in the microscopic PFM measurements and could not obtain more direct evidence for ferroelectricity from macroscopic *P*–*E* measurements because of the large leakage current under high DC electric field (data not shown).

## Discussion

First, we discuss the origin of the classical ferroelectricity in the present films. It is plausible that the domains exhibiting classical ferroelectricity can be classified as the polar *trans*-type phase, considering that room-temperature ferroelectricity in the *cis*-type structures has never been observed, experimentally or theoretically. However, first-principles calculations performed by Hinuma *et al.* suggested that SrTaO<sub>2</sub>N with specific *cis*-type structures exhibits reversible polarisation, although the polarisation flips within picoseconds at room temperature<sup>23</sup>. Such a fluctuating polarisation might be frozen by the epitaxial strain from the STO substrate, but our *ab initio* molecular dynamics simulations excluded the possibility of polarisation freezing (Supplementary Fig. S4). Thus, we attribute

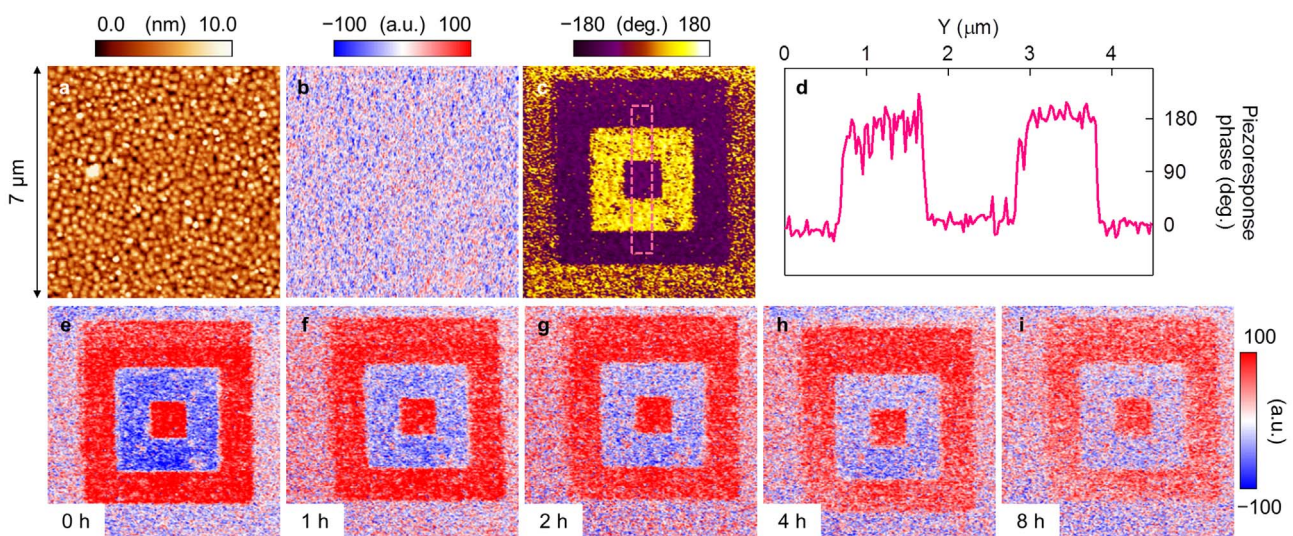


**Figure 4 | Polarisation relaxation in the  $\text{SrTaO}_2\text{N}$  epitaxial thin films.** (a) Topographic and (b) piezoresponse ( $A \cos\theta$ ) images obtained simultaneously from the  $\text{SrTaO}_2\text{N}$  thin film (thickness = 288 nm) in the virgin state. (c) Phase images of the  $\text{SrTaO}_2\text{N}$  film just after the poling process. (d) Averaged line profile of the dashed rectangle region in (c), which displays a clear  $180^\circ$  inversion of the phase. (e)–(i) Piezoresponse images obtained from the same area as (c) 1, 2, 4, and 8 hours after the poling process.

the classical ferroelectric behaviour in the small domains to *trans*-type N ordering.

Next, we validated the epitaxial stabilisation of the polar *trans*-type structure by using DFT calculations, as suggested by Page *et al.*<sup>6</sup> but not yet confirmed. We compared the energies of the three representative phases suggested by Page *et al.*: paraelectric antipolar *cis*-type (space group symmetry:  $Pbmm$ ), nonpolar *trans*-type ( $I4/mcm$ ), and ferroelectric polar *trans*-type ( $P4mm$ ) configurations (Table 1)<sup>6</sup>. Among these structures, the *cis*-type  $Pbmm$  phase was the most energetically stable, consistent with Page *et al.*<sup>6</sup>, although we could not completely reproduce the absolute values of the energy difference among these structures (see Supplementary Note). Figure 7 shows how the epitaxial stress affected the phase stability, calculating the potential energies as functions of the in-plane lattice constant (Supplementary Fig. S5). Remarkably, as the in-plane lattice parameters decreased, the paraelectric *cis*-type  $Pbmm$  phase became much less stable, regardless of the crystallographic orientation, while the stability of the *trans*-type structures only decreased a small amount. This finding implies that the compressive strain along the

in-plane direction stabilised the polar *trans*-type nitrogen arrangement relative to the *cis*-type.

Note that the *cis*-type  $Pbmm$ -X phase was more stable than the *trans*-type phases, even under compressive strain (Fig. 7). Considering the major distribution of the relaxor-like phase in the  $\text{SrTaO}_2\text{N}$  film (Fig. 3b and 4b), the relaxor-like phase may be attributable to the  $Pbmm$ -X phase or to a mixture of the *cis*-type phases; we attribute the minor classical ferroelectric phase to the *trans*-type  $P4mm$  phase. Contrasting the classical ferroelectricity originating from atomic displacement in the *trans*-type phase, the origin of the relaxor-like properties in the *cis* phases is still unclear. However, the lack of long-range atomic order, a common characteristic of relaxor ferroelectric materials<sup>20</sup>, may play a role in the relaxor-like behaviour. These results will stimulate future work to explain the relationship

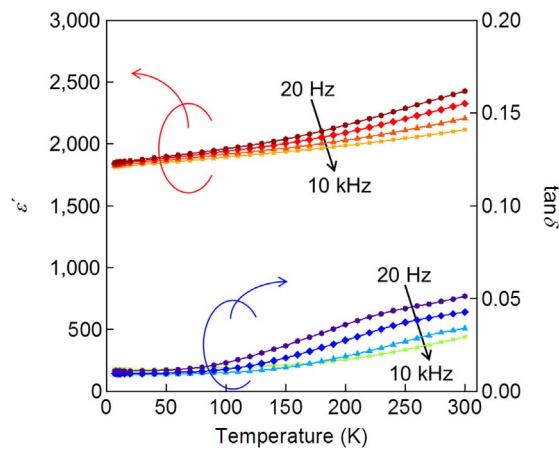


**Figure 5 | Temperature dependence of the dielectric constant of the  $\text{SrTaO}_2\text{N}$  epitaxial thin film.** The dielectric constants and  $\tan\delta$  of the  $\text{SrTaO}_2\text{N}$  film (thickness = 288 nm) measured at 20 Hz, 100 Hz, 1 kHz, and 10 kHz as a function of temperature.

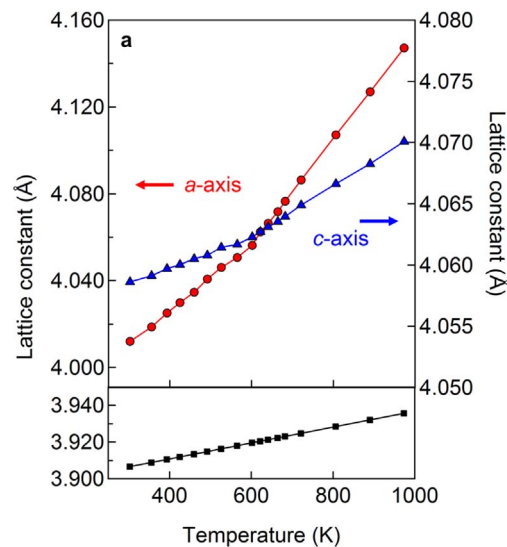


**Figure 6 | Temperature dependence of the lattice constants of the  $\text{SrTaO}_2\text{N}$  epitaxial thin film.** (a) The *a*- and *c*-axis lattice constants of the  $\text{SrTaO}_2\text{N}$  film (thickness = 100 nm) capped with an amorphous  $\text{LaAlO}_3$  protection layer and (b) simultaneously measured lattice constant of Nb-doped  $\text{SrTiO}_3$  substrate as a function of temperature.



**Table 1 | Geometrically optimised crystal structures of *Pbmm cis*, *I4/mcm trans*, and *P4mm trans* models without strain. The total energy per formula unit of each structure relative to the most stable *Pbmm* phase,  $E$ , is also displayed. Structural images are shown in Fig. 7**

Polarity	<i>Pbmm cis</i>	<i>I4/mcm trans</i>	<i>P4mm trans</i>
	Antipolar	Nonpolar	Polar
$a$ (Å)	5.81783	4.00435	4.00545
$b$ (Å)	5.78146		
$c$ (Å)	4.00811	4.12524	4.30080
$E$ (meV)	0	216	211

between the anion arrangement in perovskite oxynitrides and their ferroelectric properties.

In conclusion, by using PFM we observed classical ferroelectric behaviour in compressively strained  $\text{SrTaO}_2\text{N}$  epitaxial thin films grown on STO substrates. To our knowledge, this report provides the first observation of ferroelectric behaviour in perovskite oxynitrides. Classical ferroelectricity coincident with visible light absorption is difficult to achieve with conventional perovskite oxides, making  $\text{SrTaO}_2\text{N}$  useful for ferroelectric photocatalysts<sup>24</sup> and ferroelectric-based photovoltaic cells<sup>25</sup>. We attributed the classical ferroelectricity in regions with  $10^1$ – $10^2$  nm domains to *trans*-type anion ordering, likely stabilised by compressive epitaxial strain. In contrast, the surrounding matrix region showed relaxor ferroelectric-like behaviour, characterised by the absence of spontaneous polarisation, positive  $d\epsilon'/dT$ , and a ferroelectric–paraelectric phase transition around 600 K. DFT calculations of the phase stability under epitaxial strain suggested that small domains of the *trans*-type classical ferroelectric phase were embedded in a *cis*-type relaxor-like matrix. To further study the mechanism of the observed ferroelectricity, identifying the N-site in the oxynitrides would be a challenging study. The present

study paves the way towards tailoring the functionality of perovskite oxynitrides by using epitaxial strain to modify anion arrangements.

## Methods

**Sample preparation.**  $\text{SrTaO}_{3-x}\text{N}_x$  thin films were prepared on the (100) plane of  $\text{SrTiO}_3$  single crystalline substrates by NPA-PLD using a KrF excimer laser. A  $\text{Sr}_2\text{Ta}_2\text{O}_7$  ceramic pellet was used as a target, which was prepared by a conventional solid-state reaction of  $\text{Ta}_2\text{O}_5$  and  $\text{SrCO}_3$ <sup>26</sup>. Nitrogen gas was activated by an electron cyclotron resonance (ECR) plasma source (Tectra, Gen2). The partial pressure of nitrogen gas ( $P_{\text{N}_2}$ ) was varied from  $\sim 1.00 \times 10^{-7}$  to  $1.00 \times 10^{-4}$  Torr, and the substrate temperature was set in a range from 500 to  $800^\circ\text{C}$ . The film growth rate was controlled by the laser repetition rate (0.3–20 Hz) and pulse energy (4–20 mJ). In the PFM and dielectric capacitance measurements,  $\text{SrTaO}_2\text{N}$  films deposited on conductive Nb(0.5 wt%)-doped  $\text{SrTiO}_3$  substrates were used after the following two-step heat treatments for suppressing the leakage current: (1) annealing at  $500^\circ\text{C}$  for 30 h under a gas mixture of nitrogen ( $P_{\text{N}_2} = 1.0 \times 10^{-5}$  Torr, activated by ECR) and oxygen (partial pressure of  $2.0 \times 10^{-5}$  Torr) and (2) annealing at  $320^\circ\text{C}$  for  $\sim 500$  h in air. The resultant changes in nitrogen content and lattice parameters produced by these treatments were negligible within the detection limits of NRA and XRD, respectively. To avoid oxidation, we capped the  $\text{SrTaO}_2\text{N}$  epitaxial thin films used for high-temperature XRD with an amorphous  $\text{LaAlO}_3$  layer (thickness of  $\sim 20$  nm). The cap layer was deposited by PLD at room temperature under a partial oxygen pressure of  $3.1 \times 10^{-3}$  Torr.

**Chemical composition analysis.** The nitrogen content in the films was evaluated by the NRA method using the  $^{15}\text{N}(p,\gamma\gamma)^{12}\text{C}$  resonant nuclear reaction at 898 keV. NRA measurements were carried out with a 1-MV tandemron accelerator at Tandem Accelerator Complex, University of Tsukuba. The emitted  $\gamma$ -rays were detected with two 3-inch  $\text{Bi}_4\text{Ge}_3\text{O}_{12}$  scintillation counters. The total amount of nitrogen was calculated by comparison to a reference sample (TiN thin film) under the reasonable assumption that the  $^{15}\text{N}/^{14}\text{N}$  ratio was equal to the natural isotope ratio in both the samples and the reference. The stoichiometry of the Sr and Ta in the samples, fabricated under optimised conditions, was confirmed by RBS.

**Crystal structure analysis.** The lattice parameters of the thin films were evaluated by XRD measurements with a four-axis diffractometer (Bruker AXS, d8 discover). A domed hot stage (Anton Paar, DHS 1100) evacuated with a rotary pump ( $\sim 10$  Pa) was used in the high temperature XRD measurement. A 200-kV TEM (JEOL Ltd., JEM-2010HC) and an aberration-corrected STEM (JEOL Ltd., JEM-2100F) were used for cross-sectional observations of thin specimens prepared by ion milling.

**Optical absorption spectrum.** The absorption spectrum of the  $\text{SrTaO}_2\text{N}$  films was calculated from extinction coefficients evaluated by a spectroscopic ellipsometer (J.A. Woollam, M-2000U).

**Atomic force microscopy (AFM) and PFM.** AFM and PFM measurements were conducted using a scanning probe microscope (SII-nanotechnology, E-Sweep with NanoNaviReal) with a homemade PFM system composed of a function generator (NF corporation, 1930A) and a lock-in amplifier (EG&G, 7260). An Rh-coated silicon cantilever (SII-nanotechnology, SI-DF3-R(100) with stiffness of 1.1 N/m and a resonance frequency of 25 kHz in air) was employed for the measurements. In the PFM measurements, the frequency of the driving AC electric field was set to a value slightly (less than 1 KHz) deviated from the contact resonance ( $\sim 110$  kHz). The amplitude of the driving AC field was 1 V. A domain poling process was performed using the following three steps: (1) applying a sample bias of +7 V on the central  $5 \times 5 \mu\text{m}^2$  area, (2) applying -7 V on the central  $3 \times 3 \mu\text{m}^2$  area, and (3) applying +7 V on the central  $1 \times 1 \mu\text{m}^2$  area.

**Dielectric measurements.** Dielectric constants were determined by a conventional capacitance method. Pt top electrodes ( $200 \mu\text{m}\varphi$ ) were sputtered onto the  $\text{SrTaO}_2\text{N}$  thin films. The capacitance and  $\tan\delta$  of the  $\text{SrTaO}_2\text{N}$  films were examined with a precision LCR meter (Agilent, E4980). A cryogen-free micro-manipulated probe station (Lake Shore, CRX-4K) was used for temperature control.

**DFT calculations.** The potential energy surface (PES) was calculated using Vienna *ab initio* software package. The Perdew–Burke–Ernzerhof (PBE) functional and projector-augmented wavefunction pseudopotential were adapted. The cut-off energy was 560 eV (41.2 Ry). The  $\mathbf{k}$ -points were sampled according to the Monkhorst–Pack (MP)  $8 \times 8 \times 8$  for *Pbmm* and *P4mm* cells. The MP  $8 \times 8 \times 4$  was used for *I4/mcm*. The atomic positions were optimised until the residual force acting on all atomic coordinates was less than  $0.01 \text{ eV}/\text{\AA}$ . The bottom of the PES was calculated by optimising the size and shape of the unit cell and the atomic positions. The residual pressure was smaller than  $0.035 \text{ GPa}$  in all directions for all considered anion orderings. A validity check was performed using the Quantum Espresso (QE) software package. In the case of QE, the PBE functional and ultrasoft pseudopotential were employed, and the cut-off energy was 48.0 Ry for the wavefunctions. The  $\mathbf{k}$ -points were sampled according to MP  $4 \times 4 \times 6$ , MP  $6 \times 6 \times 6$ , and MP  $6 \times 6 \times 4$  for *Pbmm*, *P4mm*, and *I4/mcm*, respectively.

1. Jansen, M. & Letschert, H. Inorganic yellow-red pigments without toxic metals. *Nature* **404**, 980–982 (2000).

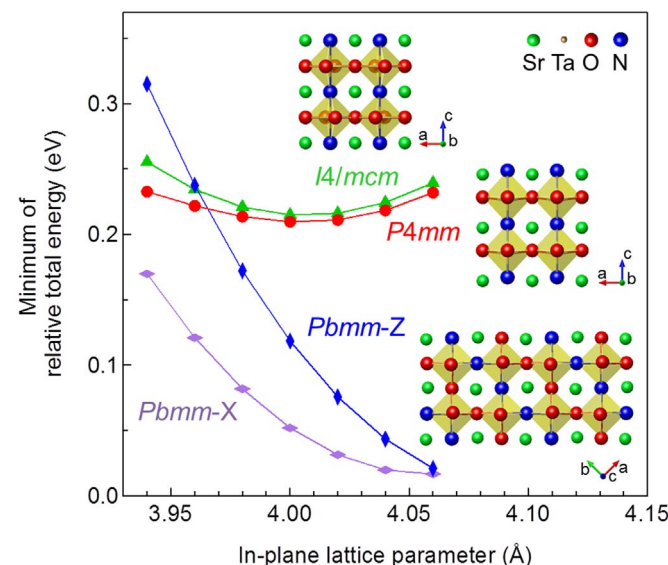


**Figure 7 | Phase stability of  $\text{SrTaO}_2\text{N}$ .** The total energy per formula unit of each structure,  $E$ , under epitaxial strain; *Pbmm cis* (diamonds, the [110] and [001] directions were assumed as the out-of-plane direction for *Pbmm-X* and *Pbmm-Z*, respectively), *I4/mcm trans* (triangles), *P4mm trans* (circles). Out-of-plane lattice constants were optimised for each point and the values of  $E$  are relative to the most stable *Pbmm* phase without strain. The structures for each model without strain drawn by VESTA<sup>27</sup> are also displayed.



2. Kasahara, A. *et al.* Photoreactions on  $\text{LaTiO}_2\text{N}$  under visible light irradiation. *J. Phys. Chem. A* **106**, 6750–6753 (2002).
3. Yang, M., Oró-Solé, J., Kusmartseva, A., Fuertes, A. & Attfield, J. P. Electronic tuning of two metals and colossal magnetoresistances in  $\text{EuWO}_{1+x}\text{N}_{2-x}$  perovskites. *J. Am. Chem. Soc.* **132**, 4822–4829 (2010).
4. Kim, Y.-I., Woodward, P. M., Baba-Kishi, K. Z. & Tai, C. W. Characterization of the structural, optical, and dielectric properties of oxynitride perovskites  $\text{AMO}_2\text{N}$  ( $\text{A} = \text{Ba, Sr, Ca; M} = \text{Ta, Nb}$ ). *Chem. Mater.* **16**, 1267–1276 (2004).
5. Fuertes, A. Chemistry and applications of oxynitride perovskites. *J. Mater. Chem.* **22**, 3293–3299 (2012).
6. Page, K. *et al.* Local atomic ordering in  $\text{BaTaO}_2\text{N}$  studied by neutron pair distribution function analysis and density functional theory. *Chem. Mater.* **19**, 4037–4042 (2007).
7. Yang, M. *et al.* Anion order in perovskite oxynitrides. *Nat. Chem.* **3**, 47–52 (2011).
8. Zhang, Y.-R., Motohashi, T., Masubuchi, Y. & Kikkawa, S. Local anionic ordering and anisotropic displacement in dielectric perovskite  $\text{SrTaO}_2\text{N}$ . *J. Ceram. Soc. Jpn.* **119**, 581–586 (2011).
9. Kim, Y.-I. *et al.* Epitaxial thin-film deposition and dielectric properties of the perovskite oxynitride  $\text{BaTaO}_2\text{N}$ . *Chem. Mater.* **19**, 618–623 (2007).
10. Jones, C. W., Battle, P. D., Lightfoot, P. & Harrison, W. T. A. The structure of  $\text{SrRuO}_3$  by time-of-flight neutron powder diffraction. *Acta Cryst. C* **45**, 365–367 (1989).
11. Marchand, R. *et al.* Perovskites oxynitrides utilisées en tant que matériaux dielectriques. *J. Phys. Colloques.* **47**, C1-901–C1-905 (1986).
12. Ebbinghaus, S. G., Aguiar, R., Weidenkaff, A., Gsell, S. & Reller, A. Topotactical growth of thick perovskite oxynitride layers by nitridation of single crystalline oxides. *Solid State Sci.* **10**, 709–716 (2008).
13. Okino, H., Sakamoto, J. & Yamamoto, T. Contact-resonance piezoresponse force microscope and its application to domain observation of  $\text{Pb}(\text{Mg}_{1/3}\text{Nb}_{2/3})\text{O}_3$ – $\text{PbTiO}_3$  single crystals. *Jpn. J. Appl. Phys.* **42**, 6209–6213 (2003).
14. Kalinin, S. V., Morozovska, A. N., Chen, L. Q. & Rodriguez, B. J. Local polarization dynamics in ferroelectric materials. *Rep. Prog. Phys.* **73**, 056502 (2010).
15. Park, M. *et al.* Piezoresponse force microscopy studies of  $\text{PbTiO}_3$  thin films grown via layer-by-layer gas phase reaction. *Appl. Phys. Lett.* **94**, 092901 (2009).
16. Kim, Y. *et al.* Origin of surface potential change during ferroelectric switching in epitaxial  $\text{PbTiO}_3$  thin films studied by scanning force microscopy. *Appl. Phys. Lett.* **94**, 032907 (2009).
17. Shvartsman, V. *et al.* Polar nanodomains and local ferroelectric phenomena in relaxor lead lanthanum zirconate titanate ceramics. *Appl. Phys. Lett.* **86**, 202907 (2005).
18. Kim, Y. *et al.* Ionically-mediated electromechanical hysteresis in transition metal oxides. *ACS nano* **6**, 7026–7033 (2012).
19. Bark, C. W. *et al.* Switchable Induced Polarization in  $\text{LaAlO}_3/\text{SrTiO}_3$  Heterostructures. *Nano Lett.* **12**, 1765–1771 (2012).
20. Bokov, A. A. & Ye, Z.-G. Recent progress in relaxor ferroelectrics with perovskite structure. *J. Mater. Sci.* **41**, 31–52 (2006).
21. Parker, R. Static dielectric constant of rutile ( $\text{TiO}_2$ ), 1.6–1060°K. *Phys. Rev.* **124**, 1719–1722 (1961).
22. Choi, K. J. *et al.* Enhancement of ferroelectricity in strained  $\text{BaTiO}_3$  thin films. *Science* **306**, 1005–1009 (2004).
23. Hinuma, Y. *et al.* First-principles study on relaxor-type ferroelectric behavior without chemical inhomogeneity in  $\text{BaTaO}_2\text{N}$  and  $\text{SrTaO}_2\text{N}$ . *Chem. Mater.* **24**, 4343–4349 (2012).
24. Inoue, Y. Photocatalytic water splitting by  $\text{RuO}_2$ -loaded metal oxides and nitrides with  $\text{d}^0$ - and  $\text{d}^{10}$ -related electronic configurations. *Energy Environ. Sci.* **2**, 364–386 (2009).
25. Yang, S. Y. *et al.* Above-bandgap voltages from ferroelectric photovoltaic devices. *Nat. nanotechnol.* **5**, 143–147 (2010).
26. Aguiar, R., Logvinovich, D., Weidenkaff, A., Reller, A. & Ebbinghaus, S. G. Thermal oxidation of oxynitride perovskites in different atmospheres. *Thermochim. Acta* **471**, 55–60 (2008).
27. Momma, K. & Izumi, F. VESTA 3 for three-dimensional visualization of crystal, volumetric and morphology data. *J. Appl. Cryst.* **44**, 1272–1276 (2011).

## Acknowledgments

We thank Mr. Seiji Ito, Mr. Akira Morita, and Prof. Katsuyuki Fukutani of the University of Tokyo and Dr. Daiichiro Sekiba of the University of Tsukuba for their assistance in the setup of the NRA measurements. We also appreciate Dr. Hitoshi Morioka of Bruker AXS for his assistance in the high-temperature XRD measurements. This study was supported by the Ministry of Education, Culture, Sports, Science, and Technology (MEXT), Japan as part of KAKENHI No. 24760005 and the Japan Society for the Promotion of Science (JSPS) KAKENHI, Grant Number No. 248258. A part of this work was conducted in Research Hub for Advanced Nano Characterization, The University of Tokyo, under the support of “Nanotechnology Platform” (project No.12024046) by MEXT, Japan.

## Author contributions

Y.H. conceived the project. D.O. and Y.H. designed the study under the supervision of T.H. D.O. synthesised the samples and characterised them by XRD. Y.H., K.S., S.I., and D.O. set up the NRA with advice from H.M., and D.O. and Y.H. conducted the measurements with the assistance of K.S. and S.I. Y.H. conducted the spectroscopic ellipsometry measurements, and Y.S. and Y.I. obtained the TEM images. PFM was set up by Y.H. and operated by D.O. D.O. conducted the dielectric capacitance measurements, and H.K. performed the first-principles calculations. D.O., Y.H., H.K., T.F., and T.H. wrote the manuscript, and all of the authors commented on the paper.

## Additional information

Supplementary information accompanies this paper at <http://www.nature.com/scientificreports/>

**Competing financial interests:** The authors declare no competing financial interests.

**How to cite this article:** Oka, D. *et al.* Possible ferroelectricity in perovskite oxynitride  $\text{SrTaO}_2\text{N}$  epitaxial thin films. *Sci. Rep.* **4**, 4987; DOI:10.1038/srep04987 (2014).



This work is licensed under a Creative Commons Attribution-NonCommercial-NoDerivs 3.0 Unported License. The images in this article are included in the article's Creative Commons license, unless indicated otherwise in the image credit; if the image is not included under the Creative Commons license, users will need to obtain permission from the license holder in order to reproduce the image. To view a copy of this license, visit <http://creativecommons.org/licenses/by-nc-nd/3.0/>